Progress in Oceanography 211 (2023) 102975

Contents lists available at ScienceDirect

Progress in Oceanography

journal homepage: www.elsevier.com/locate/pocean

Deep ocean circulation in the subpolar North Atlantic observed by acoustically-tracked floats

Sijia Zou [a,*], Amy S. Bower [b], M. Susan Lozier [c], Heather H. Furey [b]

[a] State Key Laboratory of Marine Environmental Science & College of Ocean and Earth Sciences, Xiamen University, Xiamen, China
[b] Department of Physical Oceanography, Woods Hole Oceanographic Institution, Woods Hole, MA, USA
[c] School of Earth and Atmospheric Sciences, Georgia Institute of Technology, Atlanta, GA, USA

ARTICLE INFO

Keywords:
North Atlantic deep ocean circulation
North Atlantic deep eddy kinetic energy
Overflow water pathways
Lagrangian float observations

ABSTRACT

The deep circulation in the subpolar North Atlantic determines the spread and mixing of high latitude climate signals to lower latitudes. However, our current understanding of the subpolar deep circulation has been limited due to relatively sparse observational data. To improve that understanding, we construct gridded fields of mean velocity and eddy kinetic energy (EKE) in the deep (1800–2800 dbar) subpolar North Atlantic using direct velocity measurements from 122 subsurface acoustically-tracked floats that drifted during June 2014–January 2019. The mean velocity field reveals a relatively strong deep boundary current around Greenland and in the Labrador Sea, with a weaker deep boundary current over the eastern flank of the Reykjanes Ridge, and near-zero mean flow over the western flank, implying a discontinuous deep boundary current across the subpolar basin. The deep EKE, albeit with smaller magnitudes, generally resembles the EKE pattern at the ocean surface, including relatively high values along pathways of the North Atlantic Current and west of Greenland where the Irminger Rings are formed. A surprising finding about deep EKE is an elevated band east of Greenland that parallels the coast and is not present in the surface EKE field. This high EKE band is possibly attributed to the combined influence from propagating Denmark Strait Overflow Cyclones, variability of the wind-driven recirculation offshore of southeast Greenland, and/or topographic waves. The float-based flow fields constructed in this study provide an unprecedented quantitative view of the kinematic properties of the large-scale deep circulation in the subpolar North Atlantic. Combined with cross-basin Eulerian measurements, we believe these recent observations provide a benchmark for testing and improving numerical simulations of deep ocean circulation and the Meridional Overturning Circulation, which are urgently needed for climate change predictions.

1. Introduction

Ocean circulation in the subpolar North Atlantic is a key aspect of the climate system as the currents in this region transport newly-formed deep waters equatorward as part of the Meridional Overturning Circulation. The circulation structure and variability play critical roles in modulating atmospheric carbon uptake and export in the Atlantic Ocean (Takahashi et al., 2009; Pérez et al., 2013; Gruber et al., 2019; Brown et al., 2021), and the meridional redistribution of heat and salt (Talley, 2003; Trenberth and Fasullo, 2017; Lozier et al., 2019; Li et al., 2021). Compared to knowledge of the circulation at the ocean surface, which is advantaged by satellite observations (e.g. Häkkinen and Rhines, 2004; Foukal and Lozier, 2017) and surface drifter data (e.g. Fratantoni, 2001; Brambilla and Talley, 2006; Lumpkin and Johnson, 2013), we know less about the circulation at depth due to relatively sparse observations. While acoustically-tracked and profiling float-derived velocity vectors have advanced our knowledge of the mean circulation and its variability in the upper to intermediate depths (<1800 m; Lavender et al., 2000; Fischer and Schott, 2002; Bower et al., 2002; Lankhorst and Zenk, 2006; Fischer et al., 2018), we lack similar analyses for deeper waters. As a result, descriptions of the large-scale circulation in the deep subpolar North Atlantic (≥1800 m) have been pieced together from hydrographic transects (McCartney 1992; Kieke and Rhein, 2006; Sarafanov et al., 2012; Daniault et al., 2016; Petit et al., 2018; Petit et al., 2022) and moored current meter arrays (Dickson and Brown, 1994; Saunders, 1994, 1996; Kanzow and Zenk, 2014; Bower and Furey, 2017; Zantopp et al., 2017; Hopkins et al., 2019; Pacini et al., 2020), the latter mostly confined to the topographic boundaries of the basin.

* Corresponding author.
E-mail address: szou@xmu.edu.cn (S. Zou).

https://doi.org/10.1016/j.pocean.2023.102975
Received 16 August 2022; Received in revised form 6 January 2023; Accepted 20 January 2023
Available online 28 January 2023

The deep circulation in the subpolar North Atlantic carries waters that overflow into the subpolar basin via the Greenland-Iceland-Scotland (GIS) ridge. These waters are produced by open-ocean convection (Schlosser et al., 1991) and/or transformation of Atlantic waters at intermediate depths in the Nordic Seas (Eldevik et al., 2009). The waters that feed into the North Atlantic on the western and eastern sides of Iceland are known as the Denmark Strait Overflow Water (DSOW) and Iceland-Scotland Overflow Water (ISOW), respectively (Fig. 1**a**). Downstream of the GIS ridge, these overflow waters descend the continental slopes with significant modifications of their properties and enhanced transports due to vigorous mixing and entrainment with ambient waters (Price and Baringer, 1994; Rudels et al., 2002; Girton and Sanford, 2003; Mauritzen et al., 2005; Voet and Quadfasel, 2010; Fer et al., 2010; North et al., 2018; Johns et al., 2021). Since ISOW entrains relatively warm and salty subpolar mode water in the Iceland Basin, it is identified as a bottom plume with characteristically high salinities along the eastern flank of the Reykjanes Ridge (Fig. 1**b and c**). Further downstream, ISOW is mixed and entrained with other subpolar waters, including modified Labrador Sea Water, older overflow waters, and Antarctic Bottom Water from mid-latitudes (McCartney, 1992), and gradually decreases its salinity by the time it reaches the Irminger and Labrador basins. The product of entrainment therein is often referred to as the North East Atlantic Deep Water (NEADW; Lazier et al., 2002; Hopkins et al., 2019) or the Gibbs Fracture Zone Water (Stramma et al., 2004), which generally occupies the density layer between 27.80 and 27.88 kg/m^3 (Fig. 1**b and c**). Below the NEADW layer ($\geq$27.88 kg/m^3), a colder and fresher DSOW plume blankets the bottom slope east of Greenland (Bacon and Saunders, 2010; Hopkins et al., 2019) and in the Labrador Sea (Pickart et al., 2002; Pacini et al., 2020).

Past studies have suggested that after entering the North Atlantic, overflow waters travel as a continuous deep boundary current around the topographic rim of the three subpolar basins (Iceland, Irminger and Labrador). These views have been heavily influenced by moored current observations along the boundaries, such as southwest of Iceland (Saunders, 1996; Kanzow and Zenk, 2014), within the Charlie-Gibbs Fracture Zone (Saunders, 1994; Bower and Furey, 2017), around Greenland (Dickson and Brown, 1994; Bacon and Saunders, 2010; Hopkins et al., 2019) and at the exit of the Labrador Sea (Fischer et al., 2010). However, recent observational and modeling studies have revealed important alternative pathways for the deep waters under the influence of topographic fractures in the Reykjanes Ridge (Petit et al., 2018; Furey et al., 2019; Xu et al., 2010; Zou et al., 2017) and eddy activities (Gary et al., 2011; Lozier et al., 2013; Zou et al., 2020; Xu et al., 2015; Racapé et al., 2019). Emerging evidence of these pathways has challenged the representativeness of the continuous deep boundary current view and has revealed a more complex circulation structure in the deep subpolar North Atlantic.

In this study, we derive the distributions of deep mean velocity and eddy kinetic energy (EKE) from direct velocity measurements by acoustically-tracked Range and Fixing of Sound (RAFOS; Rossby et al., 1986; Ramsey et al., 2020) floats as part of the Overturning in the Subpolar North Atlantic Program (OSNAP; Lozier et al., 2017). Results

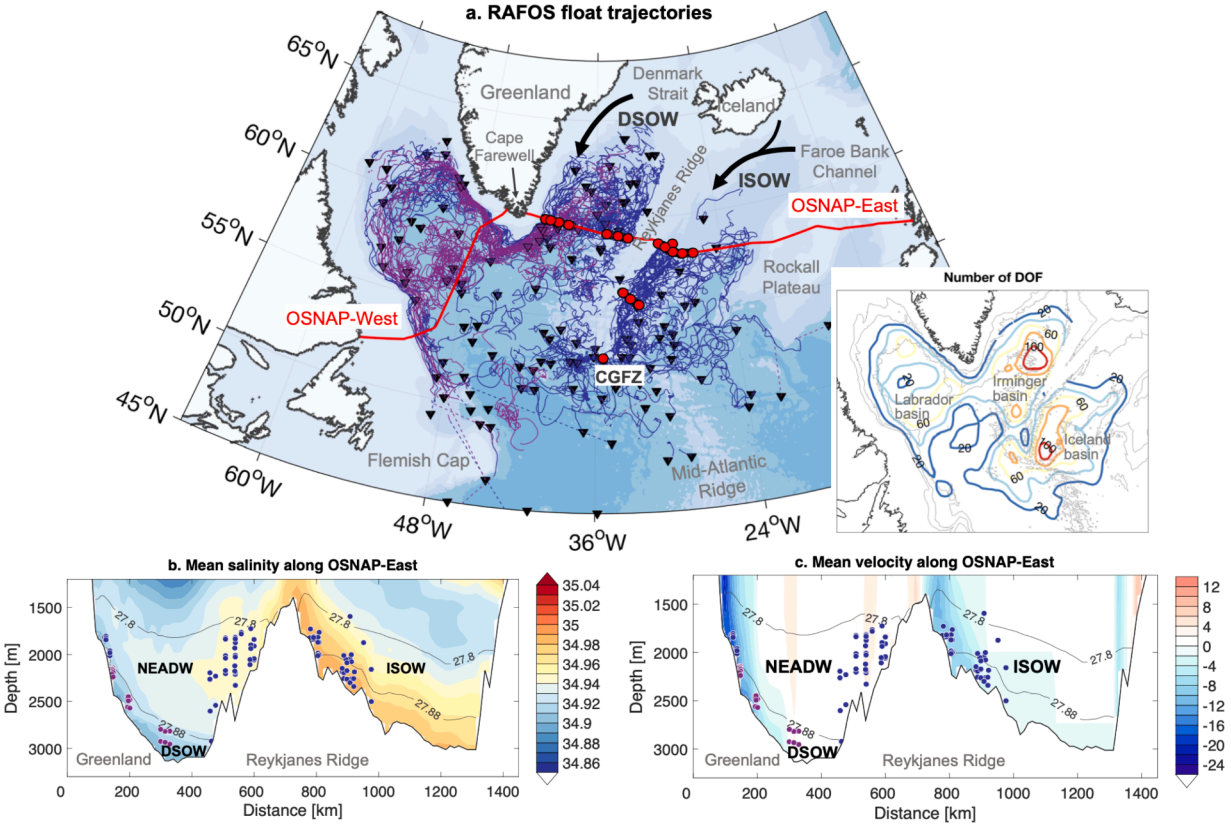

Fig. 1. **(a)** Trajectories of the OSNAP RAFOS floats. Deployment sites are indicated as red circles and end points as black triangles. Blue lines represent trajectories of 89 floats released in the ISOW/NEADW layer. Purple lines represent trajectories of 33 floats released in the DSOW layer east of Greenland. Missing trajectory segments are indicated with dashed lines. OSNAP-East and OSNAP-West sections are plotted as red lines. The 1000 m, 2000 m, 3000 m and 4000 m isobaths from ETOPO-2 are shaded in blue. **Inset**: Number of DOF based on a Lagrangian integral time scale of 4 days (Section 2.2). Contour interval is 20. **(b)** Observed mean salinity below 1200 m along OSNAP-East from August 2014 to June 2018. σ_θ of 27.80 kg/m^3 and 27.88 kg/m^3 are contoured in gray. Blue circles indicate launch locations of RAFOS floats in the ISOW/NEADW layer and purple circles indicate those in the DSOW layer east of Greenland. **(c)** Observed mean velocity below 1200 m normal to the OSNAP-East section during the same period. Acronyms in the figures: CGFZ, Charlie-Gibbs Fracture Zone; ISOW, Iceland-Scotland Overflow Water; NEADW, North East Atlantic Deep Water; DSOW, Denmark Strait Overflow Water. (For interpretation of the references to color in this figure legend, the reader is referred to the web version of this article.)

from this study provide a quantitative quasi-Eulerian view of the deep ocean circulation over a large extent of the subpolar basin, which will serve as a reference point for future studies on the deep circulation as well as on the Meridional Overturning Circulation in the North Atlantic.

2. Data and methods

2.1. RAFOS floats

RAFOS floats are neutrally buoyant drifting instruments that are tracked underwater using an array of moored sound sources (Rossby et al., 1986). Once per day, the floats listen for the acoustic signals transmitted by the sound sources and record the arrival times. At mission's end, the floats transmit these arrival times along with daily pressure and temperature measurements. Sound source transmit times, the arrival times, and climatological sound speed are used to obtain distance ranges to each source, which are in turn used to triangulate the float positions each day and construct trajectories.

During the summers of 2014–2017, the 122 RAFOS floats used in this study were deployed at five sites around the subpolar basin, with one site located east of Greenland and the other four around the Reykjanes Ridge (Fig. 1**a**). The floats were ballasted to drift at pressures between 1800 and 2800 dbar within the overflow water layer, which has historically been defined as the layer denser than 27.80 kg/m^3 (Dickson and Brown, 1994; Fig. 1**b and c**). The majority (89/122) were released in the ISOW/NEADW layer, with fewer (33/122) in the DSOW layer east of Greenland ($\geq$27.88 kg/m^3). After release, each float drifted at an approximately constant pressure level and recorded arrival times, temperature and pressure every 24 h. The nominal float mission length was 730 days, with actual record length varying from 12 days to 739 days and a mean of 637 days. The full record length spans the time period of June 2014–January 2019.

Along-track velocity is calculated by first differencing between positions that are 48 h apart, resulting in daily velocity estimates. Float position is calculated using a least-squares method (Wooding et al., 2005). Position error is estimated by combining errors from sound source and float clock with uncertainties in the sound velocity field. The sound source and float clocks accuracies are 1 s and the clocks are all independently calibrated post-mission to within a second. This translates to a ~3 km random error in float position. We combine this error with that associated with the varying sound velocity field between the float and each sound source. Position uncertainty due to anomalies in sound speed are ~2–5 km (0.01 km/s error with acoustic travel time between source and float ~5–10 min). This results in an overall position error estimate of ~5–8 km. Note, however, that the relative error between sequential positions is closer to the 3 km value since sound speed uncertainties will result in small shifts of the whole trajectory. Further details of the float dataset, including quality control and calibration procedures, can be found in Ramsey et al. (2020).

2.2. Lagrangian integral time scale

To evaluate uncertainties in statistical mappings based on the RAFOS float measurements, we calculate the Lagrangian integral time scale T_L, which estimates the time scale over which the Lagrangian velocities are correlated. Following previous studies (Taylor, 1921; Lavender et al., 2005; LaCasce, 2008), T_L is calculated by integrating the autocorrelation function of float velocity time series from zero to positive lags, i.e.

$$T_L = \int_0^{T_d} R d\tau \tag{1}$$

T_d is the de-autocorrelation time scale, representing the time when the autocorrelation function R crosses 0.

The float trajectories are first divided into 90-day continuous and non-overlapping trajectory segments. For each segment, T_L is calculated using along-track velocity time series. Among the 256 selected trajectory segments, T_L varies from 2 days to 12 days, with a mean of 4 days. In this study, we set T_L to 4 days. Compared to previous literature, T_L estimated in this study is consistent with that at 700 m in the Labrador Sea (3.8–7.7 days) based on the PALACE floats (Straneo et al., 2003) and is greater than the integral time scale estimated using isopycnal floats deployed at 27.2 and 27.5 kg/m^3 in the North Atlantic (1.5–2.5 days; Zhang et al., 2001).

2.3. Weighted Gaussian interpolation

The first approach used here to derive a gridded mean velocity field from the float measurements is the weighted Gaussian interpolation (GI). The method has been successfully applied in mapping the mean circulation pattern at intermediate depths in the subpolar gyre with Argo float data (Fischer et al., 2018) and in the deep Gulf of Mexico with acoustically-tracked floats (Pérez-Brunius et al., 2018). We first divide the study area into a regular 0.5° longitude and 0.25° latitude grid, such that the size for each grid box is ~30 km × 30 km. At each target grid point, the weighted mean velocity is calculated as

$$\overline{u^w} = \frac{\sum_{i=1}^{N} w_i u_i}{\sum_{i=1}^{N} w_i}$$

$$\overline{v^w} = \frac{\sum_{i=1}^{N} w_i v_i}{\sum_{i=1}^{N} w_i} \tag{2}$$

where N is the number of measurements near the target grid point. u_i and v_i are the i^{th} measurements and w_i is their weight, which is defined through a Gaussian function,

$$w = e^{-\left[\left(\frac{\Delta x}{L_x}\right)^2 + \left(\frac{\Delta y}{L_y}\right)^2 + \frac{(\Delta q)^2}{2\overline{q^2}}\right]} \tag{3}$$

x and y represent the zonal and meridional directions, respectively. q is the barotropic potential vorticity (PV), which is calculated as $q = f/H$, with f denoting planetary vorticity and H representing the water depth. Δx and Δy denote the distances between the target grid point and the measurement in x and y directions, respectively. L_x and L_y are the half-width of the Gaussian function and are determined by the zonal and meridional decorrelation length scales. The best fit of the correlation function for zonal and meridional velocities yields $L_x = L_y = 30$ km (**Fig. S1**). In our calculations, we increase the scales to $L_x = L_y = 40$ km to enlarge the search area and to incorporate more data for a statistically meaningful estimate. This is especially helpful in areas where measurements are relatively sparse. The resultant mean velocity field is not sensitive to this scale change. Δq of the last term in Eq. (3) is the PV difference between the target grid point and the measurement, i.e. $\Delta q = q_{target} - q_i$, and $\overline{q^2}$ is the averaged PV squared between the locations, i.e. $\overline{q^2} = \frac{1}{2}(q_{target}^2 + q_i^2)$. This last term in Eq. (3) represents a topographic constraint on the weighting function, because the deep flow is significantly steered by bathymetry in the subpolar region.

In short, at each target grid point, we search for available measurements within a horizontal radius of 80 km ($2 \times L_x$) and calculate the weighted mean by considering both the horizontal and the PV distances from the target grid point. The number of velocity measurements used for each grid box exceeds 200 in most of the areas, with a mean of 247 averaged among all grid boxes (not shown). The number of degrees of freedom (DOF) for the unweighted calculation is estimated as the number of independent measurements N_{ind} that are at least T_L days apart (Pérez-Brunius et al., 2018). For example, with T_L set as 4 days, if 10 floats visit the same grid box within 4 days, the number of DOF is 1. If 10 floats visit the same box every 4 days consecutively, the number of DOF is 10. The number of DOF in each grid box varies from 2 to 120, with a mean of 28 averaged among all grid boxes (Fig. 1**a inset**). The least

sampled regions (DOF < 20) include the northern Iceland Basin, the central Labrador Basin, and the area between the southern tip of Greenland and northeast of Flemish Cap.

When weights are taken into consideration, the number of DOF decreases such that the number of effective DOF (Kirchner, 2020) is

$$\mathrm{DOF_{eff}} = \frac{\left(\sum_{i=1}^{N_{ind}} w_i\right)^2}{\sum_{i=1}^{N_{ind}} w_i^2} \tag{4}$$

$\mathrm{DOF_{eff}}$ varies from 1 to 50, with a mean of 8 averaged over all grid boxes (not shown).

The estimated standard error of the weighted mean zonal velocity (Bevington, 1969) is

$$\mathrm{SE_u^w} = \sqrt{\frac{\mathrm{var_u^w}}{\mathrm{DOF_{eff}}}} \tag{5}$$

where $\mathrm{var_u^w}$ is the weighted variance and is calculated as

$$\mathrm{var_u^w} = \frac{\sum_{i=1}^{N} w_i (u_i - \overline{u^w})^2}{\sum_{i=1}^{N} w_i} \frac{\mathrm{DOF_{eff}}}{\mathrm{DOF_{eff}} - 1} \tag{6}$$

The weighted mean meridional velocity and its variance are calculated similarly to (5) and (6). After obtaining the mean velocity fields $\overline{u^w}$ and $\overline{v^w}$ at the target grid point, we calculate EKE as

$$\mathrm{EKE} = \frac{\sum_{i=1}^{N} (u_i - \overline{u^w})^2 + (v_i - \overline{v^w})^2}{2N} \tag{7}$$

2.4. Objective analysis

The second approach used to derive the gridded mean velocity field is the objective analysis (OA), which has been widely used in meteorology and oceanography to map spatially irregular data onto a regular grid (Gandin, 1965; Bretherton et al., 1976; Freeland and Gould, 1976; Hiller and Käse, 1983; Davis, 1998; Gille, 2003). The basis for OA is the Gauss–Markov theorem with *a priori* covariance of the signal field and the noise level of the data. If the covariance is estimated from the data itself, as opposed to an estimate based on historical data or preconceived notions, the mapping is optimal by minimizing error in the least-squares sense (Thomson and Emery, 2014).

Before objective mapping, the mean velocity field is roughly estimated and subtracted from the float measurements, because the method relies on covariance of anomalies. After mapping, the mean field is added back to the output. Here we briefly describe OA mapping of the zonal velocity (u) at a target grid point. The mapping of the meridional velocity (v) is conducted in a similar way.

The objective estimate of the zonal velocity at a target grid point is given by

$$\hat{u} = P^u (A^u + \epsilon^u I)^{-1} \phi^u \tag{8}$$

ϕ^u is a column vector containing the zonal velocity measurements, i.e.

$$\phi^u = [u_1, u_2, u_3, \cdots, u_N]^T \tag{9}$$

P^u is defined as a vector containing covariance between the target grid point and each measurement,

$$P^u = \overline{u(\phi^u)^T} \tag{10}$$

where $P_i^u = \overline{uu_i}$, $1 \le i \le N$. A^u is the covariance matrix which contains covariance between measurements, i.e.

$$A^u = \overline{\phi^u (\phi^u)^T} \tag{11}$$

where $A_{ij}^u = \overline{u_i u_j}, 1 \le i,j \le N$.

The correlation function F used is the same Gaussian function in Eq. (3). The covariance function is therefore

$$F^u = \mathrm{var_u}\, F, \text{ where } \mathrm{var_u} = \frac{1}{N} \sum_{i=1}^{N} (u_i)^2. \tag{12}$$

To represent the difference between instantaneous data and the smoothed field, a noise variance ϵ^u is added to matrix A^u,

$$\epsilon^u = r\, \mathrm{var_u} \tag{13}$$

where r represents the noise to signal ratio and has dimensions of $N \times N$. In order to take DOF into consideration, we follow previous studies (Lumpkin and Johnson, 2013; Laurindo et al., 2017) and estimate r as

$$r = \cos\left(\frac{\pi\tau}{2T_d}\right) e^{-\left(\frac{\pi\tau}{2T_d}\right)^2} \tag{14}$$

τ denotes separation time between each pair of measurements and T_d is the de-autocorrelation time scale, which is about twice T_L. By this definition, measurements that are less than T_L days apart are not fully independent. In addition, the off-diagonal values of r is multiplied by 0.9, under the assumption that 10% of the variance is due to white noise and is not correlated between measurements (Laurindo et al., 2017).

The expected error variance for estimated $\hat{u}$ is,

$$\epsilon^u = \overline{(u - \hat{u})^2} = \mathrm{var_u} - P^u (A^u + \epsilon^u I)^{-1} (P^u)^T \tag{15}$$

Roughly, a successful mapping requires an overall expected error variance to be less than 50% of the variance of the total field (Hiller and Käse, 1983). In our application, we find an unsuccessful mapping, i.e. large expected error, mostly along the rim of the subpolar basin, in the northern Iceland Basin, in the central Labrador Sea and north of the Flemish Cap. These areas are co-located with regions where measurements (DOF) are sparse. Finally, with the mean velocity estimates, EKE is calculated in the same way as Eq. (7).

2.5. Methods validation and uncertainty evaluation

Before applying weighted GI and OA to the RAFOS float data, we test both approaches with simulated float trajectories calculated using velocity field from a high-resolution ocean general circulation model. As shown in the **Supplementary Information**, the constructed velocity and EKE fields derived from both approaches compare reasonably well with those from the model's velocity output. For example, the spatial correlation between GI (OA) based velocity field and model's velocity output is 0.71 (0.74) and the spatial root mean square difference is 3.2 (3.2) cm/s. The spatial correlation of EKE between GI (OA) result and model output is 0.64 (0.67). The spatial root mean square difference of EKE is 20.9 (19.2) $\mathrm{cm^2/s^2}$ between GI (OA) result and model output. All correlation coefficients reported here and hereafter are significant at the 95% confidence level.

As pointed out by Laurindo et al. (2017), the analytically computed standard error for a quasi-Eulerian field may only account for half of the real error. We evaluate the uncertainties associated with the derived velocity field from GI (OA) in the model and find that they are very likely underestimated by a factor of 2 (1.5) (**Supplementary Information**), consistent with Laurindo et al. (2017). To account for this underestimate, we multiply the standard error $\mathrm{SE^w}$ derived from GI by 2 and the expected error $\sqrt{\epsilon}$ derived from OA by 1.5. This multiplication is done both for the model results and for those based on the RAFOS floats, under the assumption that the underestimated factors derived from the model results also apply to observations. The final estimates of uncertainties associated with the GI- and OA-based mean velocity fields are shown in Figures S2-3. Based on these results, we keep our focus on regions with relatively low uncertainties and more reliable estimates. For GI, these regions correspond to where effective DOF are >8 (non-hatched regions in Fig. 2**a**). For OA, these regions correspond to where the expected error variances are smaller than 50% of the total field

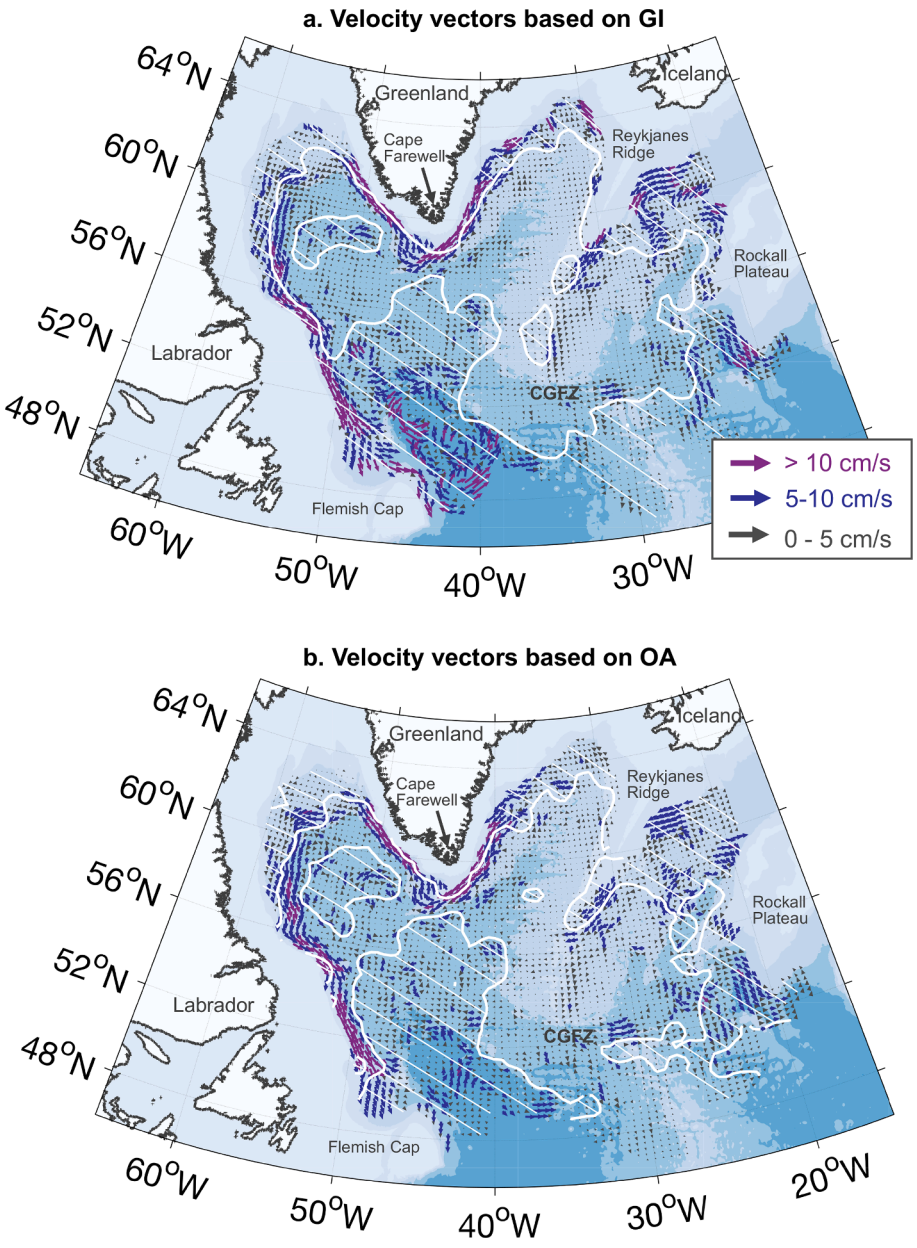

Fig. 2. Gridded mean velocity vectors in the deep (1800–2800 dbar) subpolar North Atlantic, color coded by the velocity magnitudes. **(a)** Derived from weighted GI. White hatching covers regions where effective DOF are less than 8. **(b)** Same as **(a)** but derived from OA. White hatching denotes regions where expected error variances exceed 50% of the total field variance, suggesting that the estimates are not reliable. It is noted that regions with large error variance (OA method) are approximately where the number of effective DOF is limited (GI method).

variance (non-hatched regions in Fig. 2**b**).

3. Gridded deep velocity field

The gridded mean velocity vectors derived from the RAFOS float data using GI and OA approaches are shown in Fig. 2. Both panels show topographically-steered boundary currents around Greenland, along the Labrador coast and over the eastern flank of the Reykjanes Ridge. Relatively weak recirculation branches and "semi-permanent" eddies (on the 4-year time scale) are observed in the basin interior. The spatial correlation between the two fields is 0.83 and the correlation increases to 0.95 if excluding regions with unreliable estimates (hatched regions in Fig. 2).

We further compare the GI- and OA-derived velocity fields with moored current meter measurements along the OSNAP line (more details in **Supplementary Information**). Results from both approaches compare fairly well with mooring data in terms of the flow direction and relative current speed. The spatial correlation between GI (OA) result and the OSNAP moored data is 0.83 (0.78), with a root mean square difference of 4.9 cm/s (5.4 cm/s). In the following sections, we primarily discuss the velocity field derived from OA because it provides a formal estimate of the uncertainties. Results from GI yield similar conclusions with slight differences in terms of the derived velocity magnitudes.

3.1. The Iceland and eastern Irminger basins

In the Iceland Basin, a mean southward boundary current along the eastern flank of the Reykjanes Ridge carries ISOW from 59°N (the OSNAP-East line where floats were released) to the latitude of the Charlie-Gibbs Fracture Zone at ~53°N (Fig. 2). The mean current speed along this path is greatest at 59°N, which is ~10 cm/s according to the OA result. The current speed decreases southward to ~2 cm/s near 56°N, south of which it increases to ~5 cm/s.

Near Charlie-Gibbs Fracture Zone, the deep boundary current splits into three branches (Fig. 3**a**). One of them travels eastward (with a mean current speed varying from 2 to 10 cm/s) and later bifurcates into a northward subbranch (2–6 cm/s) towards the interior Iceland Basin and a southward subbranch (1–3 cm/s) along the eastern flank of the Mid-

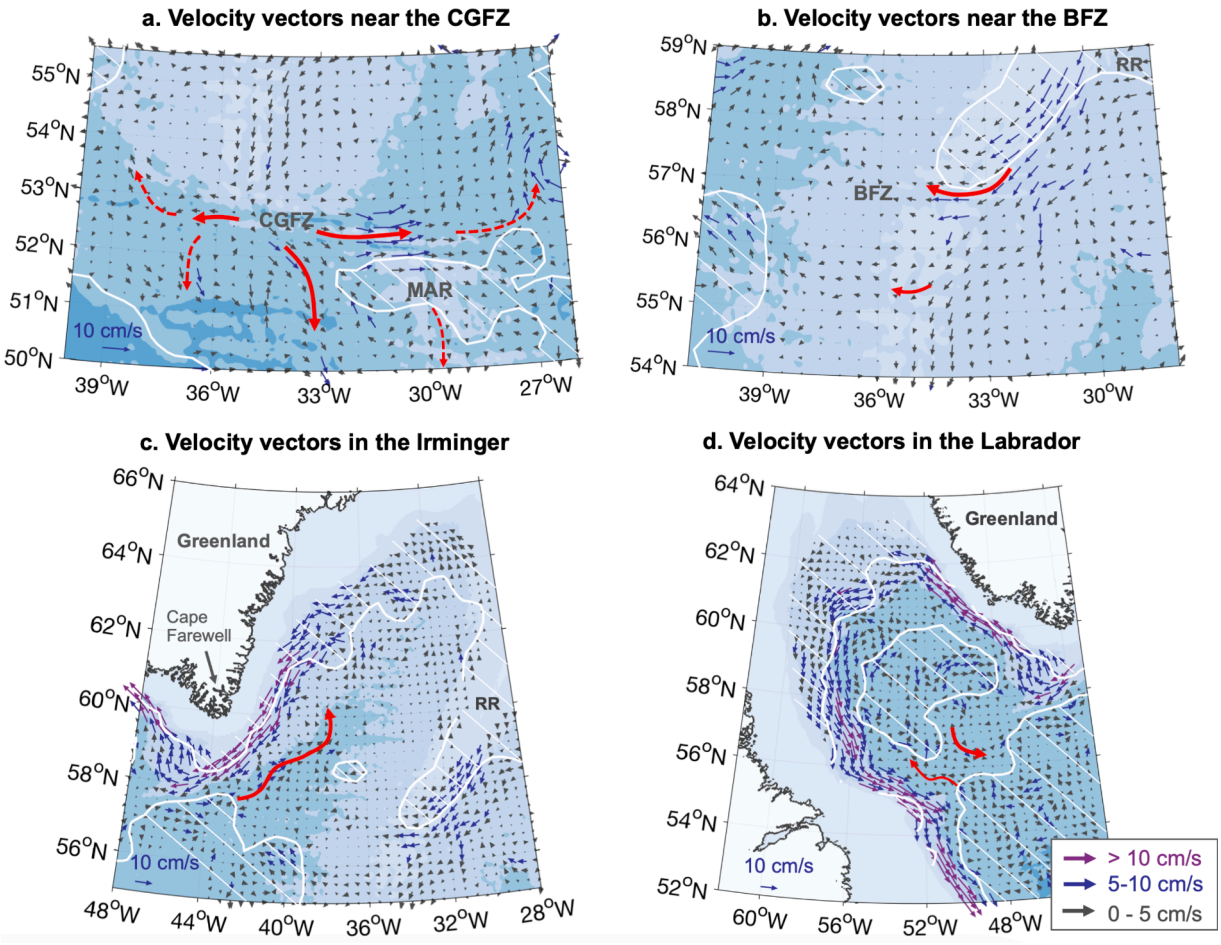

Fig. 3. **(a)** OA-based mean velocity vectors near the Charlie-Gibbs Fracture Zone. Red solid curves illustrate the three major branches in the area: an eastward, southward and westward branch. Subbranches for the eastward and westward branches are indicated as red dashed curves. MAR: Mid-Atlantic Ridge. **(b)** Mean velocity vectors near the Bight Fracture Zone (BFZ). Red solid curves denote pathways through fractures in the Reykjanes Ridge (RR). **(c and d)** Mean velocity vectors in the Irminger and Labrador basins, with red curves illustrating the recirculation branches. In all plots, velocity vectors are color-coded according to their magnitudes. (For interpretation of the references to color in this figure legend, the reader is referred to the web version of this article.)

Atlantic Ridge. The second branch from the Charlie-Gibbs Fracture Zone exhibits a direct southward spreading by crossing the fracture zone meridionally into the eastern Newfoundland Basin, west of the Mid-Atlantic Ridge. The mean current speed for this branch varies from 2 to 6 cm/s.

The third branch is directed westward through the Charlie-Gibbs Fracture Zone (~3 cm/s), which has been considered as one of the major routes for ISOW to enter the western subpolar basin (Saunders, 1994; Bower and Furey, 2017). The estimated mean speed is smaller than previous current meter observations, which showed a mean speed exceeding 4 cm/s in the ISOW layer across the Charlie-Gibbs Fracture Zone and a maximum of ~8.0 cm/s near the bottom (Bower and Furey, 2017). The difference between float and current meter measurements may be attributed to the under-sampling of the bottom intensified velocity by floats, which were mostly released at depths 100–200 m above the sea floor. Another possible explanation is the different sampling time periods between the floats (2014–2018) and the current meters (2010–2012), as the deep flow is known to be highly variable under the influence of the North Atlantic Current (NAC; Bower and Furey, 2017; Xu et al., 2018). Indeed, during 2014–2018, the eastward-flowing NAC is located further north than that during 2010–2012, which is implied from higher surface EKE and stronger eastward surface velocity near the Charlie-Gibbs Fracture Zone according to satellite altimetry data (**Fig. S4**). As such, there is a stronger eastward flow in the upper layer of the fracture zone, which possibly suppresses the westward deep flow during this time period. Lastly, and perhaps mainly, these differences can be attributed to the fact that the float-based gridded field is constructed from spatial interpolation which smooths some of the meridional structure of the zonal flow in the narrow fracture zone. After travelling through the Charlie-Gibbs Fracture Zone, this third branch of ISOW (now also considered NEADW) is shown to split into one subbranch that flows northwestward (Stramma et al., 2004; Xu et al., 2010; Zou et al., 2020) and another subbranch that flows southward into the Newfoundland Basin (Zou et al., 2020; Fig. 3**a**). The partitioning between the northwestward and the southward subbranches is shown to be influenced by the eddies and meandering activities associated with the NAC (Zou et al., 2020).

These pathways stand in contrast to historical views that suggested a direct northward ISOW/NEADW branch along the western flank of the Reykjanes Ridge after flowing through the Charlie-Gibbs Fracture Zone (e.g. Dickson and Brown, 1994; Schott et al., 1999; Daniault et al., 2016). Based on the gridded velocity map, we further confirm the absence of a robust northward boundary current by revealing a minimal flow speed ($\leq$2 cm/s) along the western flank of the Reykjanes Ridge from 53°N to 60°N (Fig. 2).

Without a direct northward pathway of ISOW from the Charlie-Gibbs Fracture Zone, where does the relatively high salinity patch, denoting the presence of ISOW, west of the Reykjanes Ridge (Fig. 1**b**) originate from? Modeling studies suggest that some ISOW could take an indirect route to reach west of the Reykjanes Ridge from the Charlie-Gibbs

Fracture Zone: after flowing northwestward towards the southern tip of Greenland, an ISOW branch turns clockwise into the central Irminger Sea, where some ISOW is able to reach the western flank of the Reykjanes Ridge (Xu et al., 2010; Zou et al., 2020; Lozier et al., 2022). However, the mean time for this simulated indirect pathway is longer than 6 years (Zou et al., 2020), suggesting that ISOW taking this route could encounter persistent mixing along the path and gradually lose its high salinity signal by the time it reaches the western flank of the Reykjanes Ridge.

A more direct route that carries ISOW to the western flank of the Reykjanes Ridge is through fracture zones in the ridge. The Bight Fracture Zone, located between 56.5°N and 57°N along the ridge (Fig. 3**b**), is one of the major fractures through which ISOW escapes into the Irminger Sea from the Iceland Basin according to float observations (Zou et al., 2017; Lozier et al., 2022), hydrographic transects (Xu et al., 2010; Petit et al., 2018; Petit et al., 2022), moorings (Furey et al., 2019) and numerical simulations (Xu et al., 2010; Zou et al., 2017; Lozier et al., 2022). The sill depth in the fracture zone is ~1850 m in the northern channel and ~2040 m in the southern channel according to ETOPO-2. The gridded mean current speed through the fracture zone is 4–6 cm/s. Another important fracture zone along the ridge is located between 55°N and 56°N, where the sill depth is ~2400 m (Petit et al., 2018) and the mean current speed is 1–2 cm/s. These direct pathways through the fracture zones are shown to be preferred by the shallower component of ISOW from the Iceland Basin according to float observations and model simulations (Zou et al., 2017; Lozier et al., 2022). By taking these more direct routes (compared to the one through the Charlie-Gibbs Fracture Zone), ISOW is more likely to preserve its high salinity when it reaches the western Reykjanes Ridge.

An alternative approach to identify the origin of ISOW over the western flank of the Reykjanes Ridge is to track the high salinity signatures using climatological data from the World Ocean Database (Fig. 4). Immediately north of the Charlie-Gibbs Fracture Zone at 54°N, a high salinity patch is observed west of the ridge (red square in Fig. 4**a**). This patch, centered at 39-40°W, resides within densities between 27.85 and 27.88 kg/m^3, denoting the northwestward pathway of ISOW from the Charlie-Gibbs Fracture Zone shown in Fig. 3**a**. Importantly, this salinity signature quickly decays northward (Fig. 4**b–d**), implying an absence of a coherent current carrying ISOW northward along the western flank of the Reykjanes Ridge. Instead, ISOW further north in the Irminger Sea enters the basin via fractures in the ridge, including the abovementioned fracture zone at ~55°N and the Bight Fracture Zone at ~57°N (red circles in Fig. 4). High salinity ISOW from the Iceland Basin spreads through these fractures into the Irminger Basin, with a slight descent down the topographic slope of the ridge. This ISOW patch generally resides within densities between 27.80 and 27.85 kg/m^3, lighter than the ISOW from the Charlie-Gibbs Fracture Zone, as expected since the lighter elements of this water mass are more likely to pass across the ridge (Zou et al., 2017).

It is important to point out that ISOW from the Iceland Basin is not the only origin of deep waters west of the Reykjanes Ridge. By backward-tracking simulated particles in high resolution ocean models, Lozier et al. (2022) conclude that only 30–40% of the deep waters west of the ridge can be traced to the Iceland Basin within 10 years. The remaining is found to originate from other subpolar basins, including the Labrador, Irminger and Newfoundland basins, and is likely a mixture of waters of different origins (Racapé et al., 2019).

3.2. *The western Irminger and Labrador basins*

In the western Irminger Sea, a narrow and strong southwestward boundary current is observed east of Greenland, extending from 62°N to the southern tip of Greenland and into the Labrador Sea (Fig. 3**c and d**). The gridded flow speed along this path varies spatially from 6 cm/s to 18 cm/s. By the time the current reaches ~62°N west of Greenland, it widens and slows down as it encounters a gentler topographic slope on

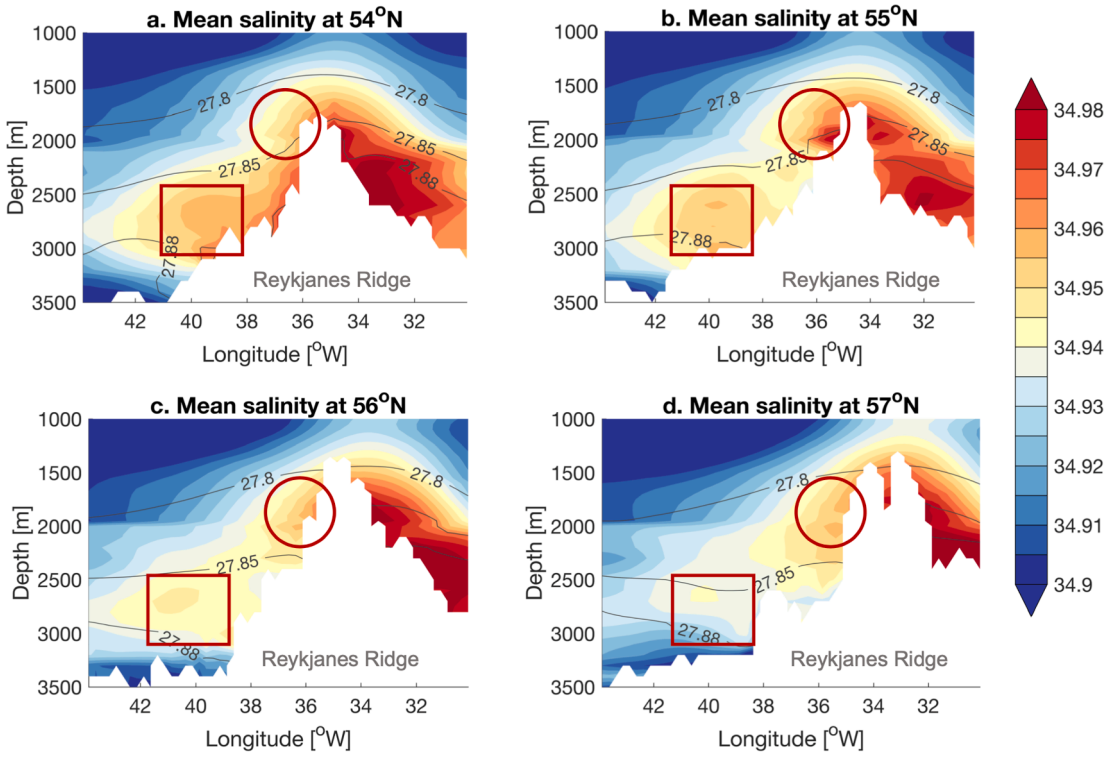

Fig. 4. Zonal climatological salinity sections at **(a)** 54°N, **(b)** 55°N, **(c)** 56°N and **(d)** 57°N over the western flank of the Reykjanes Ridge. Climatological isopycnals are contoured in gray. Red squares denote ISOW that originates from the Charlie-Gibbs Fracture Zone and circles denote ISOW from fractures in the ridge. Data is from the World Ocean Atlas (Boyer et al., 2018). (For interpretation of the references to color in this figure legend, the reader is referred to the web version of this article.)

its path around the basin, where the current speed is <6 cm/s. Once the boundary current approaches the Labrador coast, it becomes narrow and intensifies as the topographic slope steepens. The current speed along this path is generally >10 cm/s. Adjacent to the deep boundary current, relatively weak recirculation segments are observed in the Labrador Sea (Fig. 3**d**). A more coherent recirculation branch is present in the western Irminger Sea: it first travels northeastward along the 3000 m isobath until ~60°N, beyond which it flows inshore to cross the 3000 m isobath and re-joins the deep boundary current (Fig. 3**c**). Current speeds for these recirculation branches are generally weak (<6 cm/s).

Finally, between the exit of the Labrador Sea and northeast of the Flemish Cap (~50°N), the topography varies significantly and the gridded mean velocity fields become spatially variable (Fig. 2). This area coincides with the energetic northwest corner of the NAC, which has a strong barotropic component (Lazier, 1994). However, caution is needed when interpreting these velocity estimates because float measurements in this highly-variable area are quite sparse, yielding relatively large estimate errors.

4. Gridded deep EKE field

By subtracting the gridded mean velocity field from the daily float measurements, we derive the deep EKE field. Results based on GI (**Fig. S5**) and OA (Fig. 5) are quite similar, with a spatial correlation of 0.94 and spatial root mean square difference of 9.8 cm^2/s^2. It is noted that the derived EKE is relative to the space–time averaged mean flow, which not only reflects eddy motions at fixed locations but also the mesoscale spatial structure of the time-mean flow (Davis, 1998). That being said, the spatial distribution of EKE derived from float measurements compares remarkably well with that based on OSNAP current meter measurements: the spatial correlation between GI (OA) result and mooring data is 0.94 (0.92), and the spatial root mean square difference is 9.3 cm^2/s^2 (10.4 cm^2/s^2). More details on the comparison can be found in the **Supplementary Information**. In the following sections, we primarily discuss the EKE field derived from OA and focus on regions with relatively reliable estimates (i.e. non-stippled regions in Fig. 5).

4.1. The Iceland and eastern Irminger basins

EKE in the Iceland and eastern Irminger basins is weak overall (≤30 cm^2/s^2) compared to the other subpolar regions (Fig. 5**a**). An exception is in the eastern Iceland Basin at ~25°W where enhanced EKE (~70 cm^2/s^2) is observed. This area is co-located with the northeastward-flowing branch of the NAC and has been shown to be frequently occupied by eddies according to altimetry and glider observations (Zhao et al., 2018a), as well as high-resolution ocean models (Zou et al., 2017; Xu et al., 2018; Zhao et al., 2018b). The eddies are formed by barotropic and baroclinic instabilities, and are critical for the meridional heat transport variability on intra-seasonal and interannual time scales in the subpolar North Atlantic (Zhao et al., 2018a, Zhao et al., 2018b). Another region with elevated EKE, albeit of smaller magnitude, is located within and south of the Charlie-Gibbs Fracture Zone. EKE with magnitudes of 25–50 cm^2/s^2 extends zonally from west of the fracture zone (38°W) to southwest of Rockall Plateau (20°W; Fig. 5**b**). This EKE band underlies the eastward-flowing NAC and likely indicates the deep-reaching influence of the eddy and meandering activities associated with the NAC

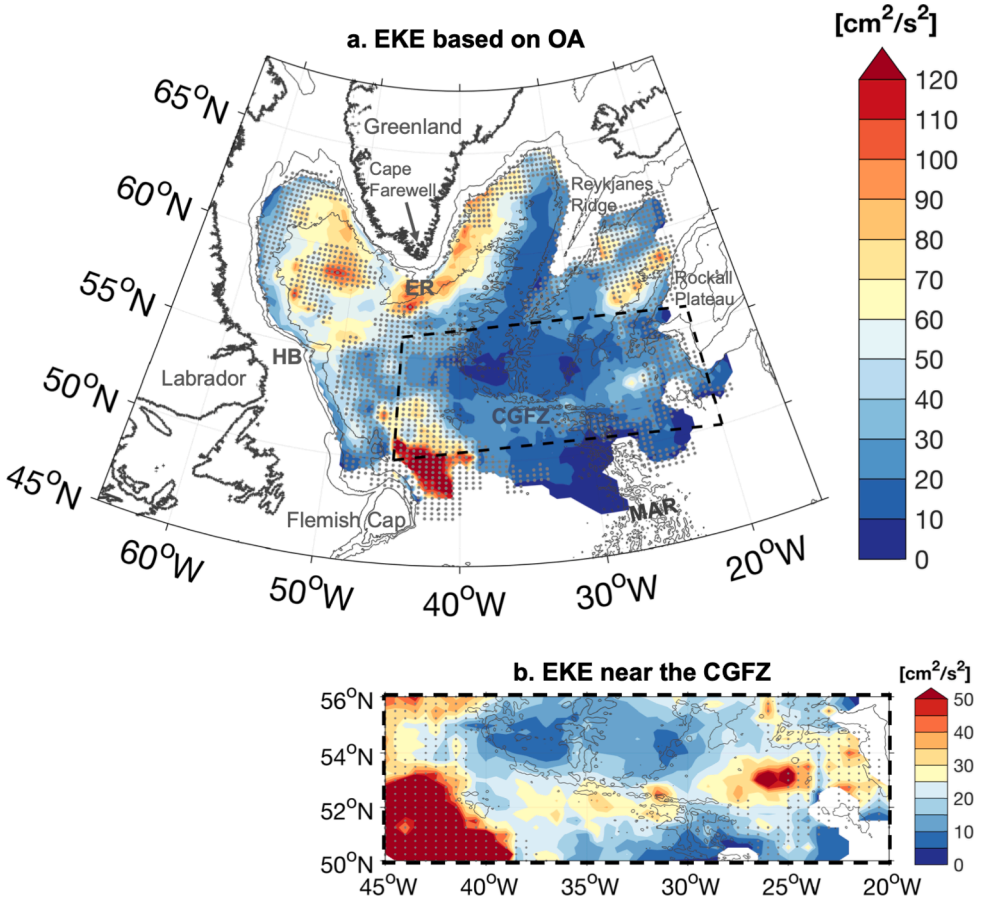

Fig. 5. (a) Gridded EKE in the deep (1800–2800 dbar) subpolar North Atlantic derived from OA. Gray dots denote areas with unreliable estimates. The 1000 m, 2000 m and 3000 m isobaths are contoured in gray. HB: Hamilton Bank; ER: Eirik Ridge. **(b)** Enlarged EKE distribution near the Charlie-Gibbs Fracture Zone, an area enclosed by the black dashed box in **(a)**. Note the different color scale used in this figure.

on the deep current variability (Saunders, 1994; Bower and Furey, 2017; Xu et al., 2018; Zou et al., 2020).

4.2. The western Irminger and Labrador basins

In the western Irminger and Labrador basins, EKE is overall stronger (50–110 cm^2/s^2) than that in the Iceland and eastern Irminger basins. An interesting EKE distribution is observed east of Greenland, where a band of elevated EKE (60–100 cm^2/s^2) between 2000 m and 3000 m isobaths extends from ~ 64°N to south of Cape Farewell. There are a number of transient processes that may contribute to this enhanced deep EKE band. First and foremost, recent observations have revealed numerous deep cyclonic eddies propagating along segments of the path of the boundary current between southwest of Denmark Strait and the vicinity of Cape Farewell (von Appen et al., 2014; Zou et al., 2021; Pacini et al., 2021). Using numerical simulations, these cyclones are shown to be formed by vortex stretching associated with the descending overflow water from the Greenland-Iceland sill (Spall and Price, 1998; Käse et al., 2003) and/or with the baroclinic instability of the overflow plume (Smith, 1976; Jungclaus et al, 2001). While the cyclonic eddies are observed to be intensified at mid-depth, they exhibit a significant bottom expression. A recent study shows that the averaged velocity anomaly in the deep overflow water layer introduced by the propagating cyclones is about 10 cm/s, according to RAFOS float and moored current meter data (Zou et al., 2021). We suggest that these cyclones are partially responsible for the elevated EKE over the slope east of Greenland. The elevated EKE may also be attributed to variability of the recirculation branch adjacent to the deep boundary current in the western Irminger Sea in response to the cyclonic wind stress curl east of Greenland (Spall and Pickart, 2003). In addition to the mechanisms mentioned above, topographic Rossby waves (Fischer et al., 2015), temporal and spatial variation of the deep boundary current, and other unknown variability/noise may also contribute to the EKE distribution.

At the southern end of the Eirik Ridge, which is the sedimentary ridge extending from Cape Farewell, EKE is even higher (>100 cm^2/s^2) compared to that east of Greenland. This is likely associated with variability in the retroflection of the boundary currents (Holliday et al., 2007) as well as the "leakage" of cyclones into the basin interior at the sharp topographic curvature of the ridge. The loss of cyclones at Eirik Ridge is supported by several RAFOS float trajectories (Zou et al., 2021) and is consistent with Pacini et al. (2021), who have revealed fewer cyclonic eddies along west Greenland than along east Greenland.

In the central-northern Labrador Sea (north of 59°N), a patch of relatively high EKE (60–90 cm^2/s^2) is observed. This deep EKE pattern mimics its surface counterpart (to be discussed in **section 5**), but with smaller magnitudes. It is primarily attributed to the eddies generated by the barotropically and/or baroclinically unstable West Greenland Current due to the varying topographic slope (e.g. Eden and Böning, 2002; Lilly et al., 2003; Bracco et al., 2008; Rieck et al., 2019). These eddies, often referred to as Irminger Rings, have surface-intensified anti-cyclonic rotations that may extend below 2000 dbar (de Jong et al., 2014). After formation, some eddies travel downstream along the isobaths while others drift offshore into the central Labrador Sea, possibly generating cyclonic rotations during their detachment from the boundary (Bracco et al., 2008) and introducing deep velocity anomalies. In addition, long-lived propagating Denmark Strait Overflow Cyclones from east of Greenland and boundary current eddies (both cyclonic and anti-cyclonic), formed at the unstable density front between the boundary current and interior Labrador Sea (de Jong et al., 2016; Gelderloos et al, 2011; Spall, 2004), could also contribute to the high EKE west of Greenland. These eddies generally travel northwestward along the boundary current towards the northern Labrador Sea, where they turn cyclonically and spread with the fanning bathymetry (de Jong et al., 2016).

Another area with relatively high EKE (60–80 cm^2/s^2) in the Labrador Sea is near the basin's exit at 56°N and 50°W. After carefully examining float trajectories in this area, we find that the high EKE is associated with the offshore deflection of a few floats near the Hamilton Bank, where relatively sharp bathymetric curvature of the 3000 m isobath is present. After the floats drifted into the basin interior from this promontory, some of them traced small anti-cyclonic loops/cusps with a mean looping radius of ~5 km. These loops/cusps are likely associated with convective eddies that were previously observed at similar locations (Lilly and Rhines, 2002). The convective eddies have been shown to form at the baroclinically unstable density front between the convective interior and the boundary current (e.g. Jones and Marshall, 1993; Rieck et al., 2019), and they were observed to exhibit anti-cyclonic rotation that could extend from near-surface to depths >2500 m (Lilly and Rhines, 2002; Lilly et al., 2003). In addition, some floats traced larger anti-cyclonic mesoscale eddies (radius ~15–40 km) that could be generated when the deep boundary current separates from the topography near Hamilton Bank. The exact formation process awaits further investigation.

Finally, an expected high EKE (>120 cm^2/s^2) patch is observed northeast of the Flemish Cap, where the NAC's Northwestern Corner is located and the flow is known to be highly variable (Lazier, 1994). Due to overall sparse measurements in this region, the derived EKE is not considered further in our discussion.

5. Comparing deep EKE with surface and mid-depth EKE

5.1. Between deep and surface EKE

The deep EKE distribution derived from the OSNAP RAFOS floats is further compared to EKE at surface and mid-depth. The surface EKE used is this study is based on the gridded daily velocity measurements by surface drifters (Fig. 6**a**; Lumpkin and Johnson, 2013; Laurindo et al., 2017). We also construct surface EKE with gridded daily geostrophic velocity derived from satellite altimetry (**Fig. S6**). While the spatial pattern of surface EKE is similar between the two datasets (spatial correlation is 0.90), the altimetry-based EKE magnitude is at least 4 times smaller than that based on drifters, which has also been illustrated in a previous study by Burkholder and Lozier (2011). This difference could be attributed to the absence of the ageostrophic velocity component (e.g. the Ekman velocity) and/or the relatively low mesoscale resolution capability of the altimetry data (Dufau et al., 2016).

At the ocean surface, elevated EKE is observed along the zonal extension of the NAC, along the NAC's northward branch west of the Rockall Plateau, and along the Irminger Current west of the Reykjanes Ridge. A high EKE patch is also observed in the central-northern Labrador Sea, where the Irminger Rings are formed (Eden and Böning, 2002; Lilly et al., 2003; Bracco et al., 2008).

The surface EKE is compared to the deep EKE derived from the RAFOS floats (Fig. 6**b**). Albeit with smaller magnitude, deep EKE distribution resembles its surface counterpart in a number of regions, including elevated EKE along the NAC zonal extension, along its northward branch west of Rockall Plateau, and in the central-northern Labrador Sea. It is therefore suggested that in these regions, while eddy activities are surface intensified, they exhibit significant influence on deep flow variability. In contrast, the relatively high surface EKE along the Irminger Current west of the Reykjanes Ridge (≥200 cm^2/s^2) is not observed at depth. The deep EKE magnitude in this area is almost the smallest (≤20 cm^2/s^2) compared to the other subpolar regions, implying that the upper ocean mesoscale activities are less deep-reaching here. Another distinct feature of the deep EKE distribution is the elevated EKE band east of Greenland, where its magnitude is comparable to the surface EKE (Fig. 7, note that ratio is on a log scale). It is implied that velocity variability in this area is very likely barotropic, which is consistent with our conjecture on the overflow cyclones, (long) topographic waves, and recirculation variability as the major perturbation processes since

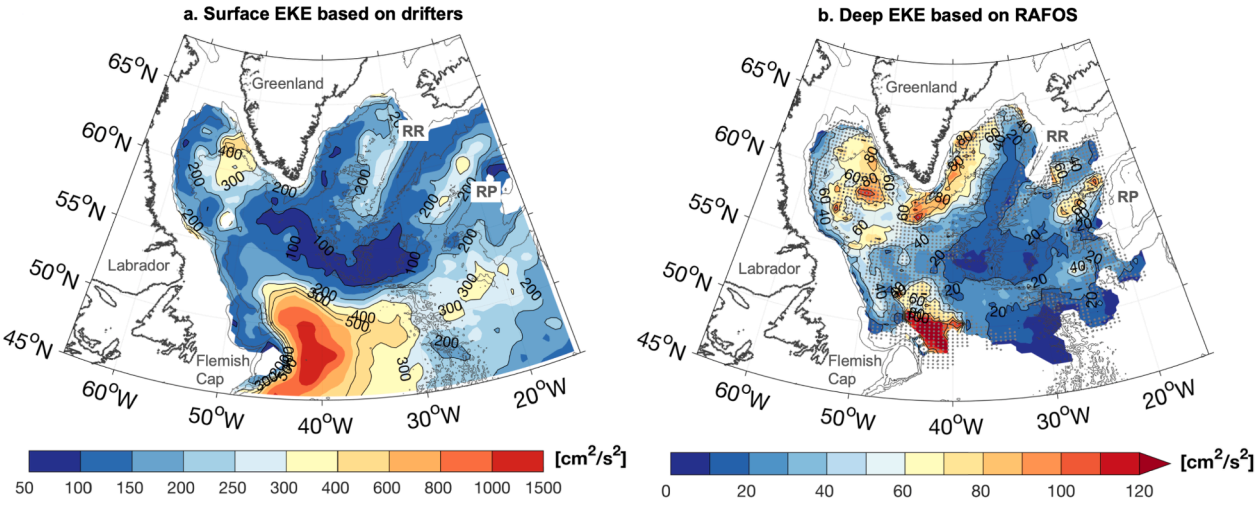

Fig. 6. **(a)** Surface EKE based on global drifter dataset. Only areas with bottom depths >1000 m are shown. **(b)** Deep EKE based on RAFOS floats (same plot as Fig. 5**a**). Note the color scale difference between **(a)** and **(b)**. RP: Rockall Plateau. 1000 m, 2000 m and 3000 m isobaths are contoured in gray.

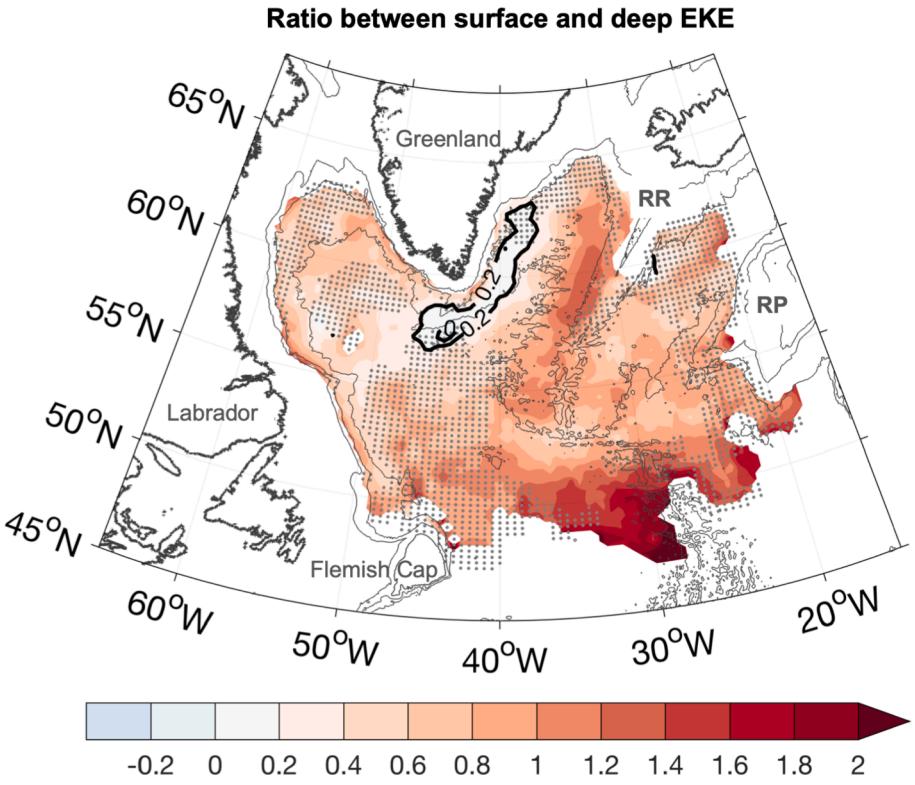

Fig. 7. Ratio (on log scale) between surface EKE (Fig. 6**a**) and deep EKE (Fig. 6**b**).

all exhibit nonnegligible barotropic components (Zou et al., 2021; Pacini et al., 2021; Fischer et al., 2015; Spall and Pickart, 2003). Because of the spatial differences mentioned above, the correlation between surface EKE and deep EKE is not significant.

5.2. Between deep and mid-depth EKE

Using velocity measurements from Argo floats, Fischer et al. (2018) constructed an EKE map at mid-depths between 1000 and 1500 m. The mid-depth EKE distribution (Fig. 8**a**) is overall similar to the deep EKE constructed in this study (spatial correlation coefficient: 0.58), but with a smaller magnitude. This is because the temporal resolution of Argo float velocity measurements is relatively coarse (10-day) compared to the RAFOS floats (daily), such that high frequency variability cannot be resolved.

In order to make a direct comparison between mid-depth and deep EKE, we low-pass filter the RAFOS float velocities with a fifth-order Butterworth filter with a cutoff period of 11 days, to mimic the Argo sampling rate before applying OA. The resultant deep EKE magnitude (Fig. 8**b**) is smaller than that based on non-filtered trajectories (Fig. 6**b**). Compared to the EKE at mid-depth, deep EKE based on low-pass filtered trajectories has comparable, or even greater, magnitude in regions with surface-intensified mesoscale activities, including the NAC's zonal extension, its northward branch west of Rockall Plateau and the central-northern Labrador Sea. East of Greenland between 2000 m and 3000 m isobaths, the deep EKE (40–60 cm^2/s^2) is much higher than the mid-

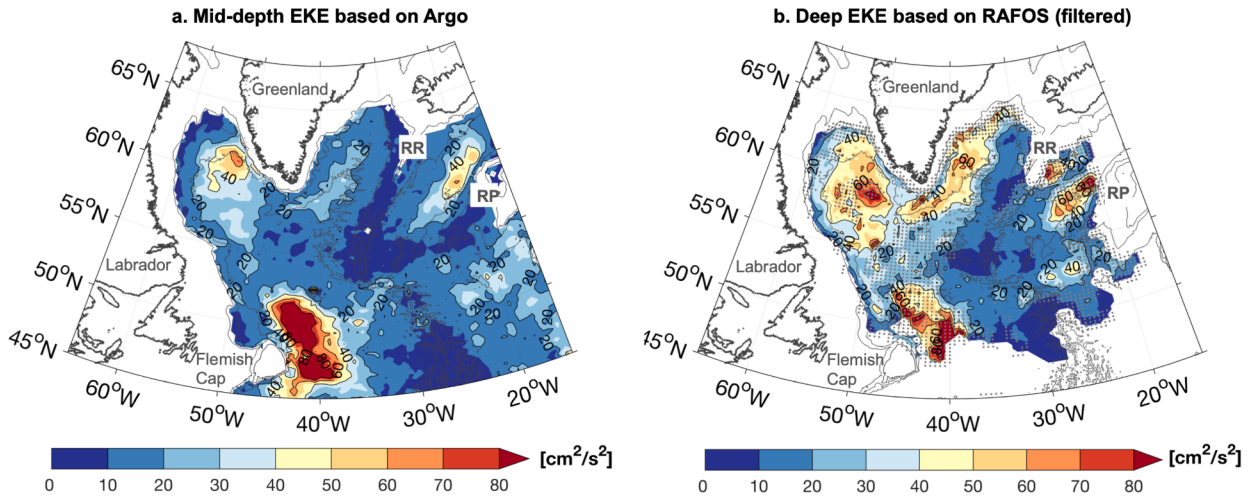

Fig. 8. **(a)** Mid-depth EKE based on Argo floats (Fischer et al., 2018). **(b)** Deep EKE based on low-pass filtered (cutoff period: 11 day) RAFOS float trajectories.

depth EKE (10–20 cm^2/s^2). It is difficult to ascertain the source of this difference: whether it is due to an actual difference of EKE between the two layers; or it is associated with the different gridding and filtering procedures applied. Due to this lack of attribute, we choose not to make further quantitative comparisons between mid-depth and deep EKE fields.

6. Caveats

Because of the limited number of RAFOS floats and nonuniform deployments/measurements, we note a number of caveats with respect to the gridded maps constructed in this study. First, the gridded maps do not resolve the vertical structure of the flow field. As shown in Fig. 1**c**, velocity is bottom intensified in the DSOW layer, which has been illustrated in a number of previous studies using moored measurements on both sides of Greenland and at the exit of the Labrador Sea (e.g. Fischer et al., 2010; Hopkins et al., 2019; Pacini et al., 2020). While it is ideal to characterize circulation features in different vertical layers, the small number of floats drifting in the DSOW layer precludes statistically reliable estimates in that layer. In addition, modeling studies suggest that the general behavior of NEADW and DSOW spreading pathways in the western subpolar basin is qualitatively similar (Lozier et al., 2022). As a result, we construct circulation maps collectively without differentiating between the two layers.

Another caveat is that the floats unevenly sample the ocean in time, possibly resulting in biased estimates if seasonal or interannual variability of the deep flow is significant. For example, all floats were released in the summer (June to August) and therefore the constructed velocity field near the release site could possibly reflect circulation in the summer only.

Additionally, the floats sample the ocean nonuniformly in space. As illustrated in Davis (1991), the mean velocity deduced from a nonuniform sampling array will be biased. This bias, or array bias as named in Davis (1991), represents the down-gradient diffusive flux of floats, i.e. $U_{array} = -K \bullet \nabla \ln\Gamma$, with K denoting diffusivity and Γ denoting sampling density. As defined, U_{array} is high in regions with relatively strong gradients of sampling density and is directed towards less sampled regions, possibly introducing a spurious mean velocity as a result. To estimate U_{array}, we derive K as $3 \times 10^3\ m^2/s$ based on single particle dispersion statistics (LaCasce, 2008). Γ is represented as the distribution of independent float measurements (i.e. DOF in Fig. 1**a inset**). The resultant U_{array} is relatively high along the contour of DOF = 20 (**Fig. S7**), where sampling is the least uniform. We note that the estimated U_{array} is quite approximate because it depends on the estimate of K, which itself, as pointed out by LaCasce (2008), can be biased by nonuniform deployments. Therefore, we do not make further corrections to account for the array bias and instead keep our focus on relatively well-sampled regions (DOF > 20) and thus relatively small array bias.

Finally, we note that most of the mean velocity magnitudes derived from GI and OA are not significantly different from 0 cm/s at the 95% confidence level, except in the boundary current areas around Greenland and along the Labrador coast (**Fig. S8**). There are multiple reasons for this lack of statistical significance across some regions. Gridding tends to smooth spatially varying flow, especially along the boundary and within the narrow fracture zones, resulting in underestimated velocity magnitudes in those regions. The relatively sparse and nonuniform sampling by the floats results in large uncertainties in the interior regions, precluding statistical significance. As pointed out by Koszalka and LaCasce (2010), when grouping nonuniform measurements into bins of the same size, the statistical significance (and standard error) varies substantially among different bins because the number of measurements is limited in many bins. To reduce this spatial variation of statistical significance, a clustering algorithm that groups a specified number of measurements into each bin has been employed. More information about this algorithm can be found in Koszalka and LaCasce (2010) and Koszalka et al. (2011). Beyond methodological deficiencies, in some areas, especially in the basin interior, the real deep mean flow may indeed be quite weak and indistinguishable from 0 cm/s. As a result, we keep our focus on the spatial pattern of the gridded fields and their relative magnitudes across different basins, instead of focusing on the absolute values and their statistical significance.

7. Conclusions

Gridded mean velocity and EKE fields (30 km × 30 km) in the deep subpolar North Atlantic are constructed with direct velocity observations by 122 acoustically-tracked RAFOS floats, which drifted at pressure levels of 1800–2800 dbar from June 2014 to January 2019. We show that the historical depiction of a strong and relatively continuous deep boundary current around the subpolar topographic rim is most representative in the western subpolar North Atlantic (around Greenland and in the Labrador Sea), and less so over the eastern flank of the Reykjanes Ridge, where mean speeds are about half as strong. A coherent boundary current is almost completely absent along the western flank of the Reykjanes Ridge, suggesting a discontinuity of the deep circulation around the ridge. Alternative pathways are discussed and quantified for the deep waters exiting the Iceland Basin, including westward and southward pathways through the Charlie-Gibbs Fracture Zone, and pathways via gaps in the Reykjanes Ridge. In addition to the large-scale circulation branches, smaller-scale eddies and recirculation

branches are observed in the subpolar basin interior.

The deep EKE distribution determined from the RAFOS floats generally resembles that at the sea surface based on drifters and at mid-depth based on Argo floats. For example, a local EKE maximum is observed in the central-northern Labrador Sea, where Irminger Rings are generated. Relatively high EKE is also present along the NAC zonal extension and its northward branch west of the Rockall Plateau, implying a deep-reaching influence of eddy activity associated with the NAC. However, the high surface EKE along the Irminger Current west of the Reykjanes Ridge is not obvious at depth, possibly suggesting upper ocean trapped eddy activity in this area.

The most distinct and surprising feature of the deep EKE field is the elevated EKE band east of Greenland between the 2000 m and 3000 m isobaths. The band extends from southwest of Denmark Strait to the southern tip of Greenland and has EKE magnitude comparable to surface EKE. The elevated EKE has a number of possible attributions: the Denmark Strait Overflow Cyclones that are generated near the sill and propagate southwestwards along the boundary current, the variability of the wind-driven recirculation branch, and the topographic waves. These processes exhibit non-negligible barotropic components and are therefore able to introduce velocity anomalies throughout the water column.

The constructed flow fields in this study provide an integrated depiction of the deep ocean circulation both qualitatively and quantitatively over a large extent of the subpolar North Atlantic. These circulation maps will shed light on the pathways, variability and connectivity of the deep waters across the subpolar basin, which are fundamental for understanding the transport and mixing of climate signals in the deep ocean. They also serve as a benchmark against which numerical simulations on the Atlantic circulation, such as the Atlantic Meridional Overturning Circulation, can be tested.

Declaration of Competing Interest

The authors declare that they have no known competing financial interests or personal relationships that could have appeared to influence the work reported in this paper.

Data availability

Data used in this study is open access. The OSNAP RAFOS float dataset can be accessed at Woods Hole Open Access Server: Furey, Heather H., Ramsey, Andree L., "Overturning in the Subpolar North Atlantic Program (OSNAP) RAFOS Float Data collected between June 2014 to January 2019", 2019-08, DOI:10.26025/1912/24388, https://hdl.handle.net/1912/24388. The OSNAP gridded product can be downloaded at https://www.o-snap.org/data-access/. The World Ocean Database 2018 can be downloaded at https://www.ncei.noaa.gov/products/world-ocean-database. The drifter-derived mean surface flow fields can be accessed at https://www.aoml.noaa.gov/phod/gdp/mean_velocity.php. Surface geostrophic velocity based on satellite altimetry is downloaded at https://cds.climate.copernicus.eu/cdsapp#!/dataset/satellite-sea-level-global?tab=overview.

Acknowledgements

The authors gratefully acknowledge the support from the Physical Oceanography Program of the U.S. National Science Foundation (Grants OCE-2017522 and OCE-1756361). S. Zou thanks F. Li for helpful conversations on OA mapping, L. C. Laurindo on estimating noise variance in OA, C. Böning and A. Biastoch for sharing FLAME model output, J. He for figure modifications and T. Xie for proofreading the manuscript. Gratitude is extended to the personnel, crew, and technicians of the R/V Knorr, R/V Thalassa, CCGS Hudson, R/V Pelagia, R/V Discovery, R/V MSMerian, and R/V Armstrong, for their efforts deploying and recovering the sound source moorings, deploying the RAFOS floats, as well as collecting the OSNAP mooring and CTD data. OSNAP data were collected and made freely available by the Overturning in the Subpolar North Atlantic Program project and all the national programs that contribute to it (www.o-snap.org). The authors would also like to acknowledge two anonynous reviewers for their helpful comments on the manuscript.

Appendix A. Supplementary material

Supplementary data to this article can be found online at https://doi.org/10.1016/j.pocean.2023.102975.

References

Bacon, S., Saunders, P.M., 2010. The deep western boundary current at Cape Farewell: results from a moored current meter array. J. Phys. Oceanogr. 40 (4), 815–829.
Bevington, P.R., 1969. Data Reduction and Error Analysis for the Physical Sciences. McGraw-Hill, p. 336 pp..
Bower, A., Furey, H., 2017. Iceland-Scotland Overflow Water transport variability through the Charlie–Gibbs Fracture Zone and the impact of the North Atlantic Current. J. Geophys. Res. Oceans 122, 6989–7012.
Bower, A.S., Le Cann, B., Rossby, T., Zenk, W., Gould, J., Speer, K., Richardson, P.L., Prater, M.D., Zhang, H.M., 2002. Directly measured mid-depth circulation in the northeastern North Atlantic Ocean. Nature 419 (6907), 603–607.
Boyer, T.P., O.K. Baranova, C. Coleman, H.E. Garcia, A. Grodsky, R.A. Locarnini, A.V. Mishonov, C.R. Paver, J.R. Reagan, D. Seidov, I.V. Smolyar, K. Weathers, M.M. Zweng, 2018. World Ocean Database 2018. A.V. Mishonov, Technical Ed., NOAA Atlas NESDIS 87. <https://www.ncei.noaa.gov/sites/default/files/2020-04/wod_intro_0.pdf>.
Bracco, A., Pedlosky, J., Pickart, R.S., 2008. Eddy formation near the west coast of Greenland. J. Phys. Oceanogr. 38 (9), 1992–2002.
Brambilla, E., Talley, L.D., 2006. Surface drifter exchange between the North Atlantic subtropical and subpolar gyres. J. Geophys. Res. Oceans 111 (C7).
Bretherton, F.P., Davis, R.E., Fandry, C.B., 1976. A technique for objective analysis and design of oceanographic experiments applied to MODE-73. In: Deep Sea Research and Oceanographic Abstracts, Vol. 23(7). Elsevier, pp. 559–582.
Brown, P.J., McDonagh, E.L., Sanders, R., Watson, A.J., Wanninkhof, R., King, B.A., Smeed, D.A., Baringer, M.O., Meinen, C.S., Schuster, U., Yool, A., 2021. Circulation-driven variability of Atlantic anthropogenic carbon transports and uptake. Nat. Geosci. 14 (8), 571–577.
Burkholder, K.C., Lozier, M.S., 2011. Subtropical to subpolar pathways in the North Atlantic: deductions from Lagrangian trajectories. J. Geophys. Res. Oceans 116 (C7).
Daniault, N., Mercier, H., Lherminier, P., Sarafanov, A., Falina, A., Zunino, P., Pérez, F.F., Ríos, A.F., Ferron, B., Huck, T., Thierry, V., 2016. The northern North Atlantic Ocean mean circulation in the early 21st century. Prog. Oceanogr. 146, 142–158.
Davis, R.E., 1991. Observing the general circulation with floats. Deep Sea Res. Part A Oceanogr. Res. Papers 38, S531–S571.
Davis, R.E., 1998. Preliminary results from directly measuring middepth circulation in the tropical and South Pacific. J. Geophys. Res. Oceans 103 (C11), 24619–24639.
de Jong, M.F., Bower, A.S., Furey, H.H., 2014. Two years of observations of warm-core anticyclones in the Labrador Sea and their seasonal cycle in heat and salt stratification. J. Phys. Oceanogr. 44 (2), 427–444.
de Jong, M.F., Bower, A.S., Furey, H.H., 2016. Seasonal and interannual variations of Irminger ring formation and boundary–interior heat exchange in FLAME. J. Phys. Oceanogr. 46 (6), 1717–1734.
Dickson, R.R., Brown, J., 1994. The production of North Atlantic Deep Water: sources, rates, and pathways. J. Geophys. Res. Oceans 99 (C6), 12319–12341.
Dufau, C., Orstynowicz, M., Dibarboure, G., Morrow, R., Le Traon, P.-Y., 2016. Mesoscale resolution capability of altimetry: present & future. J. Geophys. Res 121, 4910–4927. https://doi.org/10.1002/2015JC010904.
Eden, C., Böning, C., 2002. Sources of eddy kinetic energy in the Labrador Sea. J. Phys. Oceanogr. 32 (12), 3346–3363.
Eldevik, T., Nilsen, J.E.Ø., Iovino, D., Olsson, K.A., Sandø, A.B., Drange, H., 2009. Observed sources and variability of Nordic seas overflow. Nat. Geosci. 2 (6), 406–410.
Fer, I., Voet, G., Seim, K.S., Rudels, B., Latarius, K., 2010. Intense mixing of the Faroe Bank Channel overflow. Geophys. Res. Lett. 37 (2).
Fischer, J., Schott, F.A., 2002. Labrador Sea Water tracked by profiling floats—from the boundary current into the open North Atlantic. J. Phys. Oceanogr. 32 (2), 573–584.
Fischer, J., Visbeck, M., Zantopp, R., Nunes, N., 2010. Interannual to decadal variability of outflow from the Labrador Sea. Geophys. Res. Lett. 37 (24).
Fischer, J., Karstensen, J., Zantopp, R., Visbeck, M., Biastoch, A., Behrens, E., Böning, C. W., Quadfasel, D., Jochumsen, K., Valdimarsson, H., Jónsson, S., 2015. Intra-seasonal variability of the DWBC in the western subpolar North Atlantic. Prog. Oceanogr. 132, 233–249.
Fischer, J., Karstensen, J., Oltmanns, M., Schmidtko, S., 2018. Mean circulation and EKE distribution in the Labrador Sea Water level of the subpolar North Atlantic. Ocean Sci. 14 (5), 1167–1183.
Foukal, N.P., Lozier, M.S., 2017. Assessing variability in the size and strength of the North Atlantic subpolar gyre. J. Geophys. Res. Oceans 122 (8), 6295–6308.
Fratantoni, D.M., 2001. North Atlantic surface circulation during the 1990's observed with satellite-tracked drifters. J. Geophys. Res. Oceans 106 (C10), 22067–22093.

Freeland, H.J., Gould, W.J., 1976. Objective analysis of meso-scale ocean circulation features. In: Deep Sea Res. Oceanogr. Abstr., 23(10). Elsevier, pp. 915–923.
Furey, H., Bower, A., Ramsey, A., 2019, January. Variability of the Deep Bight: Two-years of Mooring Data in the Bight Fracture Zone. In Geophysical Research Abstracts (Vol. 21).
Gandin, L.S., 1965: Objective Analysis of Meteorological Fields. Israel Program for Scientific Translations, 242 pp.
Gary, S.F., Lozier, M.S., Böning, C.W., Biastoch, A., 2011. Deciphering the pathways for the deep limb of the meridional overturning circulation. Deep Sea Res. Part II 58 (17–18), 1781–1797.
Gelderloos, R., Katsman, C.A., Drijfhout, S.S., 2011. Assessing the roles of three eddy types in restratifying the Labrador Sea after deep convection. J. Phys. Oceanogr. 41 (11), 2102–2119.
Gille, S.T., 2003. Float observations of the Southern Ocean. Part I: Estimating mean fields, bottom velocities, and topographic steering. J. Phys. Oceanogr. 33 (6), 1167–1181.
Girton, J.B., Sanford, T.B., 2003. Descent and modification of the overflow plume in the Denmark Strait. J. Phys. Oceanogr. 33 (7), 1351–1364.
Gruber, N., Clement, D., Carter, B.R., Feely, R.A., Van Heuven, S., Hoppema, M., Ishii, M., Key, R.M., Kozyr, A., Lauvset, S.K., Monaco, C.L., 2019. The oceanic sink for anthropogenic CO2 from 1994 to 2007. Science 363 (6432), 1193–1199.
Häkkinen, S., Rhines, P.B., 2004. Decline of subpolar North Atlantic circulation during the 1990s. Science 304 (5670), 555–559.
Hiller, W., Käse, R.H., 1983. Objective analysis of hydrographic data sets from mesoscale surveys.
Holliday, N.P., Meyer, A., Bacon, S., Alderson, S.G., de Cuevas, B., 2007. Retroflection of part of the east Greenland current at Cape Farewell. Geophys. Res. Lett. 34 (7).
Hopkins, J.E., Holliday, N.P., Rayner, D., Houpert, L., Le Bras, I., Straneo, F., Wilson, C., Bacon, S., 2019. Transport variability of the Irminger Sea Deep Western Boundary Current from a mooring array. J. Geophys. Res. Oceans 124 (5), 3246–3278.
Johns, W.E., Devana, M., Houk, A., Zou, S., 2021. Moored observations of the Iceland-Scotland overflow plume along the eastern flank of the Reykjanes Ridge. J. Geophys. Res. Oceans 126 (8) p. e2021JC017524.
Jones, H., Marshall, J., 1993. Convection with rotation in a neutral ocean: a study of open-ocean deep convection. J. Phys. Oceanogr. 23 (6), 1009–1039.
Jungclaus, J.H., Hauser, J., Käse, R.H., 2001. Cyclogenesis in the Denmark Strait overflow plume. J. Phys. Oceanogr. 31 (11), 3214–3229.
Kanzow, T., Zenk, W., 2014. Structure and transport of the Iceland Scotland Overflow plume along the Reykjanes Ridge in the Iceland Basin. Deep Sea Res. Part I 86, 82–93.
Käse, R.H., Girton, J.B., Sanford, T.B., 2003. Structure and variability of the Denmark Strait Overflow: model and observations. J. Geophys. Res. Oceans 108 (C6).
Kieke, D., Rhein, M., 2006. Variability of the overflow water transport in the western subpolar North Atlantic, 1950–97. J. Phys. Oceanogr. 36 (3), 435–456.
Kirchner, J., 2020. Data analysis toolkits. EnviDat. https://doi.org/10.16904/envidat.177.
Koszalka, I., LaCasce, J.H., 2010. Lagrangian analysis by clustering. Ocean Dyn. 60, 957–972. https://doi.org/10.1007/s10236-010-0306-2.
Koszalka, I., LaCasce, J.H., Andersson, M., Orvik, K.A., Mauritzen, C., 2011. Surface circulation in the Nordic Seas from clustered drifters. Deep-Sea Res. I 58, 468–485. https://doi.org/10.1016/j.dsr.2011.01.007.
LaCasce, J., 2008. Statistics from Lagrangian observations. Prog. Oceanogr. 77 (1), 1–29.
Lankhorst, M., Zenk, W., 2006. Lagrangian observations of the middepth and deep velocity fields of the northeastern Atlantic Ocean. J. Phys. Oceanogr. 36 (1), 43–63.
Laurindo, L., Mariano, A., Lumpkin, R., 2017. An improved near-surface velocity climatology for the global ocean from drifter observations. Deep-Sea Res. I (124), 73–92. https://doi.org/10.1016/j.dsr.2017.04.009.
Lavender, K.L., Davis, R.E., Owens, W.B., 2000. Mid-depth recirculation observed in the interior Labrador and Irminger seas by direct velocity measurements. Nature 407 (6800), 66–69.
Lavender, K.L., Owens, W.B., Davis, R.E., 2005. The mid-depth circulation of the subpolar North Atlantic Ocean as measured by subsurface floats. Deep Sea Res. Part I 52 (5), 767–785.
Lazier, J.R., 1994. Observations in the northwest corner of the North Atlantic Current. J. Phys. Oceanogr. 24 (7), 1449–1463.
Lazier, J., Hendry, R., Clarke, A., Yashayaev, I., Rhines, P., 2002. Convection and restratification in the Labrador Sea, 1990–2000. Deep Sea Res. Part I 49 (10), 1819–1835.
Li, F., Lozier, M., Holliday, N., Johns, W., Le Bras, I., Moat, B., Cunningham, S., de Jong, M., 2021. Observation-based estimates of heat and freshwater exchanges from the subtropical North Atlantic to the Arctic. Prog. Oceanogr. 197, 102640.
Lilly, J.M., Rhines, P.B., 2002. Coherent eddies in the Labrador Sea observed from a mooring. J. Phys. Oceanogr. 32 (2), 585–598.
Lilly, J.M., Rhines, P.B., Schott, F., Lavender, K., Lazier, J., Send, U., D'Asaro, E., 2003. Observations of the Labrador Sea eddy field. Prog. Oceanogr. 59 (1), 75–176.
Lozier, M.S., Gary, S.F., Bower, A.S., 2013. Simulated pathways of the overflow waters in the North Atlantic: subpolar to subtropical export. Deep Sea Res. Part II 85, 147–153.
Lozier, M.S., Bacon, S., Bower, A.S., Cunningham, S.A., De Jong, M.F., De Steur, L., Deyoung, B., Fischer, J., Gary, S.F., Greenan, B.J., Heimbach, P., 2017. Overturning in the Subpolar North Atlantic Program: a new international ocean observing system. Bull. Am. Meteorol. Soc. 98 (4), 737–752.
Lozier, M.S., Li, F., Bacon, S., Bahr, F., Bower, A.S., Cunningham, S.A., de Jong, M.F., de Steur, L., deYoung, B., Fischer, J., Gary, S.F., 2019. A sea change in our view of overturning in the subpolar North Atlantic. Science 363 (6426), 516–521.
Lozier, M.S., Bower, A.S., Furey, H.H., Drouin, K.L., Xu, X., Zou, S., 2022. Overflow water pathways in the North Atlantic. Prog. Oceanogr. 208, 102874.
Lumpkin, R., Johnson, G.C., 2013. Global ocean surface velocities from drifters: Mean, variance, El Niño-Southern Oscillation response, and seasonal cycle. J. Geophys. Res. Oceans 118 (6), 2992–3006.
Mauritzen, C., Price, J., Sanford, T., Torres, D., 2005. Circulation and mixing in the Faroese Channels. Deep Sea Res. Part I 52 (6), 883–913.
McCartney, M.S., 1992. Recirculating components to the deep boundary current of the northern North Atlantic. Prog. Oceanogr. 29 (4), 283–383.
North, R.P., Jochumsen, K., Moritz, M., 2018. Entrainment and energy transfer variability along the descending path of the Denmark Strait overflow plume. J. Geophys. Res. Oceans 123 (4), 2795–2807.
Pacini, A., Pickart, R.S., Bahr, F., Torres, D.J., Ramsey, A.L., Holte, J., Karstensen, J., Oltmanns, M., Straneo, F., Le Bras, I.A., Moore, G.W.K., 2020. Mean conditions and seasonality of the West Greenland boundary current system near Cape Farewell. J. Phys. Oceanogr. 50 (10), 2849–2871.
Pacini, A., Pickart, R.S., Le Bras, I.A., Straneo, F., Holliday, N.P., Spall, M.A., 2021. Cyclonic eddies in the West Greenland boundary current system. J. Phys. Oceanogr.
Pérez, F.F., Mercier, H., Vázquez-Rodríguez, M., Lherminier, P., Velo, A., Pardo, P.C., Rosón, G., Ríos, A.F., 2013. Atlantic Ocean CO 2 uptake reduced by weakening of the meridional overturning circulation. Nat. Geosci. 6 (2), 146–152.
Pérez-Brunius, P., Furey, H., Bower, A., Hamilton, P., Candela, J., García-Carrillo, P., Leben, R., 2018. Dominant circulation patterns of the deep Gulf of Mexico. J. Phys. Oceanogr. 48 (3), 511–529.
Petit, T., Mercier, H., Thierry, V., 2018. First direct estimates of volume and water mass transports across the Reykjanes Ridge. J. Geophys. Res. Oceans 123 (9), 6703–6719.
Petit, T., Thierry, V., Mercier, H., 2022. Deep through-flow in the Bight Fracture Zone. Ocean Sci. 18 (4), 1055–1071.
Pickart, R.S., Torres, D.J., Clarke, R.A., 2002. Hydrography of the Labrador Sea during active convection. J. Phys. Oceanogr. 32 (2), 428–457.
Price, J.F., Baringer, M.O.N., 1994. Outflows and deep water production by marginal seas. Prog. Oceanogr. 33, 161–200. https://doi.org/10.1016/0079-6611(94)90027-2.
Racapé, V., Thierry, V., Mercier, H., Cabanes, C., 2019. ISOW spreading and mixing as revealed by deep-argo floats launched in the Charlie-Gibbs fracture zone. J. Geophys. Res. Oceans 124 (10), 6787–6808.
Ramsey, A., Furey, H., Bower, A., 2020. Overturning of the Subpolar North Atlantic Program (OSNAP): RAFOS Float Data Report, June 2014 – January 2019. Woods Hole Oceanographic Institution Technical Report, WHOI-2020-06. doi:10.1575/1912/26515.
Rieck, J.K., Böning, C.W., Getzlaff, K., 2019. The nature of eddy kinetic energy in the Labrador Sea: different types of mesoscale eddies, their temporal variability, and impact on deep convection. J. Phys. Oceanogr. 49 (8), 2075–2094.
Rossby, T., Dorson, D., Fontaine, J., 1986. The RAFOS system. J. Atmos. Ocean. Tech. 3 (4), 672–679.
Rudels, B., Fahrbach, E., Meincke, J., Budéus, G., Eriksson, P., 2002. The East Greenland Current and its contribution to the Denmark Strait overflow. ICES J. Mar. Sci. 59 (6), 1133–1154.
Sarafanov, A., Falina, A., Mercier, H., Sokov, A., Lherminier, P., Gourcuff, C., Gladyshev, S., Gaillard, F., Daniault, N., 2012. Mean full-depth summer circulation and transports at the northern periphery of the Atlantic Ocean in the 2000s. J. Geophys. Res. Oceans 117 (C1).
Saunders, P.M., 1994. The flux of overflow water through the Charlie-Gibbs Fracture Zone. J. Geophys. Res. Oceans 99 (C6), 12343–12355.
Saunders, P.M., 1996. The flux of dense cold overflow water southeast of Iceland. J. Phys. Oceanogr. 26 (1), 85–95.
Schlosser, P., Bönisch, G., Rhein, M., Bayer, R., 1991. Reduction of deepwater formation in the Greenland Sea during the 1980s: evidence from tracer data. Science 251 (4997), 1054–1056.
Schott, F., Stramma, L., Fischer, J., 1999. Interaction of the North Atlantic current with the deep Charlie Gibbs Fracture Zone throughflow. Geophys. Res. Lett. 26, 369–372.
Smith, P.C., 1976. Baroclinic instability in the Denmark Strait overflow. J. Phys. Oceanogr. 6 (3), 355–371.
Spall, M.A., Price, J.F., 1998. Mesoscale variability in denmark strait: the PV outflow hypothesis. J. Phys. Oceanogr. 28 (8), 1598–1623.
Spall, M.A., Pickart, R.S., 2003. Wind-driven recirculations and exchange in the Labrador and Irminger Seas. J. Phys. Oceanogr. 33 (8), 1829–1845.
Spall, M.A., 2004. Boundary currents and watermass transformation in marginal seas. J. Phys. Oceanogr. 34 (5), 1197–1213.
Stramma, L., Kieke, D., Rhein, M., Schott, F., Yashayaev, I., Koltermann, K.P., 2004. Deep water changes at the western boundary of the subpolar North Atlantic during 1996 to 2001. Deep Sea Res. Part I 51 (8), 1033–1056.
Straneo, F., Pickart, R.S., Lavender, K., 2003. Spreading of Labrador sea water: an advective-diffusive study based on Lagrangian data. Deep Sea Res. Part I 50 (6), 701–719.
Takahashi, T., Sutherland, S., Wanninkhof, R., Sweeney, C., Feely, R., Chipman, D., Hales, B., Friederich, G., Chavez, F., Sabine, C., Watson, A., Bakker, D., Schuster, U., Metzl, N., Yoshikawa-Inoue, H., Ishii, M., Midorikawa, T., Nojiri, Y., Körtzinger, A., Steinhoff, T., Hoppema, M., Olafsson, J., Arnarson, T., Tilbrook, B., Johannessen, T., Olsen, A., Bellerby, R., Wong, C., Delille, B., Bates, N., de Baar, H., 2009. Climatological mean and decadal change in surface ocean pCO2, and net sea–air CO2 flux over the global oceans. Deep Sea Res. Part II 56 (8–10), 554–577.
Talley, L.D., 2003. Shallow, intermediate, and deep overturning components of the global heat budget. J. Phys. Oceanogr. 33 (3), 530–560.
Taylor, G.I., 1921. Diffusion by continuous movements. Proc. Lond. Math. Soc. 20, 196–212.
Thomson, R.E., Emery, W.J., 2014. Data Analysis Methods in Physical Oceanography. Newnes.

Trenberth, K.E., Fasullo, J.T., 2017. Atlantic meridional heat transports computed from balancing Earth's energy locally. Geophys. Res. Lett. 44 (4), 1919–1927.
Voet, G., Quadfasel, D., 2010. Entrainment in the Denmark Strait overflow plume by meso-scale eddies. Ocean Sci. 6 (1), 301–310.
von Appen, W.J., Pickart, R.S., Brink, K.H., Haine, T.W., 2014. Water column structure and statistics of Denmark Strait Overflow Water cyclones. Deep Sea Res. Part I 84, 110–126.
Wooding, C., Furey, H., Pacheco, M., 2005. RAFOS Float Processing at the Woods Hole Oceanographic Institution. Woods Hole Oceanog. Inst. Tech. Rep., WHOI-2005-02, 35 pp.
Xu, X., Schmitz Jr, W.J., Hurlburt, H.E., Hogan, P.J., Chassignet, E.P., 2010. Transport of Nordic Seas overflow water into and within the Irminger Sea: an eddy-resolving simulation and observations. J. Geophys. Res. Oceans 115 (C12).
Xu, X., Rhines, P.B., Chassignet, E.P., Schmitz Jr, W.J., 2015. Spreading of Denmark Strait overflow water in the western subpolar North Atlantic: insights from eddy-resolving simulations with a passive tracer. J. Phys. Oceanogr. 45 (12), 2913–2932.
Xu, X., Bower, A., Furey, H., Chassignet, E., 2018. Variability of the Iceland-Scotland Overflow water transport through the Charlie–Gibbs Fracture Zone: results from an eddying simulation and observations. J. Geophys Res. Oceans 123, 5808–5823.
Zantopp, R., Fischer, J., Visbeck, M., Karstensen, J., 2017. From interannual to decadal: 17 years of boundary current transports at the exit of the Labrador Sea. J. Geophys. Res. Oceans 122, 1724–1748. https://doi.org/10.1002/2016JC012271.
Zhang, Huai-Min, et al., 2001. Isopycnal lagrangian statistics from the north atlantic current RAFOS float observations. J. Geophys. Res.: Oceans 106(C7), 13817–36. Crossref. <https://doi.org/10.1029/1999jc000101>.
Zhao, J., Bower, A., Yang, J., Lin, X., Holliday, N.P., 2018a. Meridional heat transport variability induced by mesoscale processes in the subpolar North Atlantic. Nat. Commun. 9 (1), 1–9.
Zhao, J., Bower, A., Yang, J., Lin, X., & Zhou, C., 2018b. Structure and Formation of Anticyclonic Eddies in the Iceland Basin 123(8), 5341–5359.
Zou, S., Lozier, S., Zenk, W., Bower, A., Johns, W., 2017. Observed and modeled pathways of the Iceland Scotland Overflow Water in the eastern North Atlantic. Prog. Oceanogr. 159, 211–222.
Zou, S., Bower, A., Furey, H., Lozier, M.S., Xu, X., 2020. Redrawing the Iceland–Scotland overflow water pathways in the North Atlantic. Nat. Commun. 11 (1), 1–8.
Zou, S., Bower, A., Furey, H., Pickart, R., Houpert, L., Holliday, N., 2021. Observed deep cyclonic eddies around southern Greenland. J. Phys. Oceanogr.